Surfactant-Free Synthesis of the Full Inorganic Perovskite CsPbBr₃: Evolution and Phase Stability of CsPbBr₃ vs CsPb₂Br₅ and Their Photocatalytic Properties

Anna Lucia Pellegrino* and Graziella Malandrino

Read Online

ACCESS | Metrics & More | Article Recommendations | SI Supporting Information

ABSTRACT: In the present study, the successful fabrication, through a surfactant-free one-pot synthesis in ethanol solution, of the all-inorganic halide perovskite CsPbBr₃ has been achieved. The phase formation has been obtained for the first time, using the β-diketonate complexes [Pb(hfa)₂diglyme]₂ and Cs(hfa) (Hhfa = 1,1,1,5,5,5-hexafluoro-2,4-pentanedione; diglyme = 2-methoxyethyl ether) and Br₂ as the precipitating agent. The growth of CsPb₂Br₅ microcrystals has been obtained and stabilized under specific synthetic conditions, by controlling the phase transition from CsPbBr₃ to CsPb₂Br₅ as well. The entire process was operated under acid-catalyzed conditions without any need of humidity control and hazardous organic solvents. The control of the aging time and the phase stability during the heat treatment represent the key points in order to selectively and reproducibly obtain the CsPbBr₃ or CsPb₂Br₅ phases. Structural, morphological, and compositional characterizations of the final product show the formation of square microcrystals, with a grain size of up to 3 μm, of the pure and stable perovskite CsPbBr₃ phase. Finally, promising results in photocatalytic degradation tests using rhodamine B solution have been obtained under UV light (λ = 360 nm) and visible light, showing high degradation yields of up to 81.9% and 58.4% for CsPbBr₃ and CsPb₂Br₅, respectively.

KEYWORDS: cesium lead halides, perovskite, photocatalysis, microcrystals, precipitation process, metalorganic precursors, degradation test
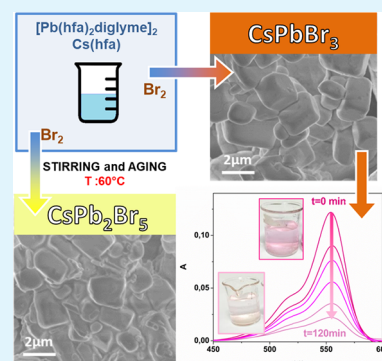
1. INTRODUCTION

The compounds belonging to the family of perovskites show a great variety of mechanical, magnetic, and optical properties[1−5] and for these reasons are currently key materials for many technologies.[6] A few examples include piezoelectrics,[7] photovoltaic solar cells,[8,9] multiferroics,[10,11] and magnetoelectrics.[12]

In the past decade, the most studied materials within the family of perovskites have been based on hybrid organic/inorganic systems with the general formula ABX₃; in particular, CH₃NH₃PbX₃ with X = Br, Cl, I have been the most investigated materials.[13,14] Since the first report of their use in solar cells,[8] the research field on hybrid perovskite solar cells (PSCs) has attracted worldwide attention, as shown by the exponential increase in the number of publications,[15−17] together with the record power conversion efficiency of 25.5%.[18]

In parallel with these interesting hybrid materials, the all-inorganic halide perovskites (AIHPs) represent an emergent class of compounds that combines the advantages of containing cheap and abundant elements with the excellent stability of these structures by excluding organic species sensitive to the external environment.[19] This class of compounds presents several functional properties,[20] such as tunable direct band gaps in the 1.5−3.2 eV range by varying the halide nature and composition,[21] large absorption coefficients, long carrier lifetimes, and high quantum efficiencies.[22] These properties make them very appealing for many applications, such as light-emitting diodes,[23,24] photodetectors,[25−27] lasers,[28] and catalysis.[29,30] Furthermore, AIHPs having an ABX₃ structure, with A = Cs, Rb, B = Pb, Sn, and X = Br, Cl, I, and the related perovskite structures AB₂X₅ and A₄BX₆ do not contain any labile or expensive components and are stable under humid conditions and a large range of temperatures even without encapsulation.[31,32] These materials have been recently applied also in aqueous medium due to their high stability as polymer-based composite systems.[33] Finally, bismuth-based halide perovskites, with the general formula A₃Bi₂X₉ (A = CH₃NH₃, Cs, Rb; X = I, Br, Cl) have attracted growing interest in the field of photovoltaics, due to their outstanding optoelectronic properties.[34,35]
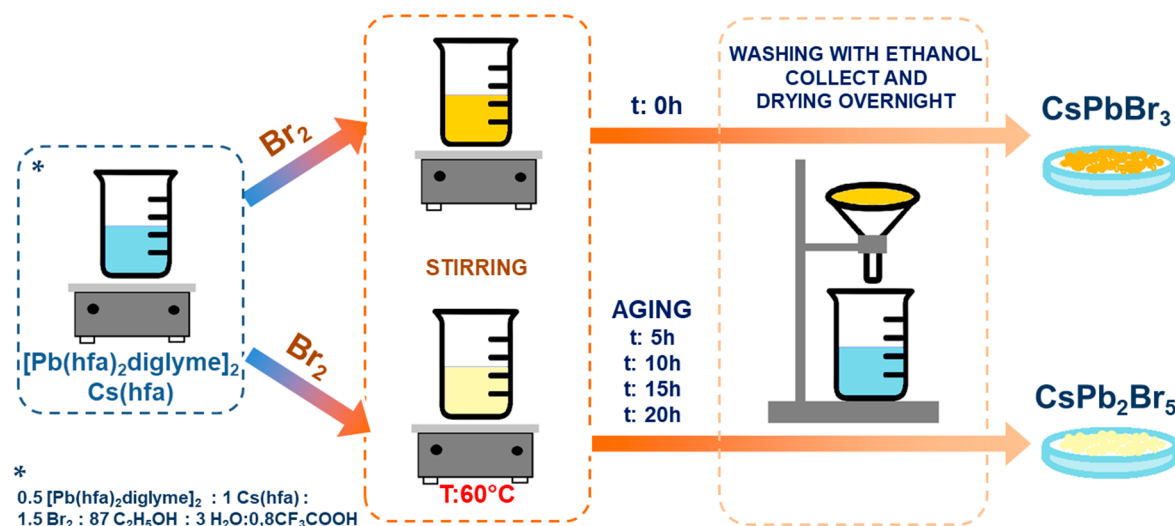
In the last few years, growing interest has been devoted to the all-inorganic perovskite-based catalysts due to their high photoluminescence[36,37] and high chemical stability.[38] In particular, one of the most emerging applications of AIHP

Scheme 1. Scheme of the CsPbBr$_3$ and CsPb$_2$Br$_5$ Synthesis at Different Aging Times

materials is with regard to the wastewater purification process of textile effluents from industrial production.[39,40] In this field, heterogeneous catalysis under light is widely accepted due to its high efficiency, yield of degradation, and cost effectiveness. Moreover, CsPbX$_3$ (X = Cl, Br, I) perovskites, in the form of quantum dots (QDs), show photoelectrochemical degradation processes of different organic dye compounds[41,42] and high performance in hydrogen evolution under visible-light irradiation.[43] In addition, it has been widely demonstrated that CsPbBr$_3$ nanocrystals are also exceptional candidates as photocatalysts for fundamental organic reactions: for example, C−C, C−N, and C−O bond formations[44] and CO$_2$ reduction.[45,46] Finally, CsPbBr$_3$ and CsPb$_2$Br$_5$ have been deeply studied as highly stable humidity sensor systems.[47]

Among the different strategies developed for the synthesis of AIHPs, surfactant-based solution routes have been widely applied, which also allow a controlled growth in the dimension and shape of the crystals.[48] The most common precursors of Cs and Pb are CsBr and PbBr$_2$, respectively,[49] which are also used in spray-coating processes for the synthesis of large-area layers.[50] However, these approaches require organic solvents, such as dimethylformamide, dimethyl sulfoxide, and toluene, and surfactant species (oleic acid and oleylamine).[19] Nevertheless, the synthetic routes using surfactants introduce additional species, which may act as contaminants during the water treatment applications and require multistep and more time-demanding procedures. These constraints may limit widespread applications in water purification, and thus research into new, facile, and green synthetic approaches is still a crucial issue.

Only few studies have reported a green approach to the synthesis of Cs-Pb-Br-based compounds. An acid-catalyzed sol−gel process was reported for the synthesis of CsPbBr$_3$/SiO$_2$ in ethanol through amine-functionalized silica micelles.[51] Cao et al. showed the formation of stable CsPbBr$_3$ films by sequential spin-coating processes using green mixed solvents.[52] CsPb$_2$Br$_5$ nanosheets have been obtained through a chemical precipitation method using a mixture of water and ethanol as the solvent, starting from PbBr$_2$ and CsBr salts.[53]

Other examples of synthesis include vapor-phase approaches, which have been tested by pulsed laser deposition,[50]

a thermal evaporation method,[54] and chemical vapor deposition.[55]

In the present paper, β-diketonate metal−organic compounds, i.e. [Pb(hfa)$_2$diglyme]$_2$ and Cs(hfa), have been for the first time applied to obtain reproducibly and selectively pure phases of CsPbBr$_3$ or CsPb$_2$Br$_5$ using Br$_2$ as a precipitating agent. The final product is influenced by the operating parameters such as aging time and heat treatment. Structural, morphological, and compositional characterizations of the final products have been addressed through X-ray diffraction (XRD), field-emission scanning electron microscopy (FE-SEM), and energy dispersive X-ray (EDX) analysis. Finally, as a proof of concept, the photocatalytic property for degradation processes has been preliminarily tested under both a UV lamp (λ 360 nm) and a visible light source using a rhodamine B dye solution.

2. EXPERIMENTAL SECTION

2.1. Synthesis Methodology. *2.1.1. Precursor Synthesis.* The complexes [Pb(hfa)$_2$·diglyme]$_2$ and Cs(hfa) were prepared following the procedures reported in refs 56 and 57, respectively, and their molecular structures are shown in Scheme S1.

2.1.2. Perovskite Synthesis. The precipitation reaction took place in an ethanol solution (volume of 5.08 mL) of Cs(hfa) (0.340 g/1 mmol) and [Pb(hfa)$_2$·diglyme]$_2$ (0.378 g/0.5 mmol) through the addition of liquid Br$_2$ (0.240 g/1.5 mmol). Trifluoroacetic acid (0.091 gr/0.8 mmol) was used as the acid catalyst.

The precursor solution with the precipitated perovskite powders was aged at 60 °C for a time range of between 0 and 20 h with stirring. The final product was collected by filtration, washed several times in ethanol, and dried overnight in air. The crystals were also subjected to an annealing treatment at 70 °C for 120 min in air.

2.2. Characterization. The crystals were deposited on Si (100) by drop-casting and analyzed by XRD in Bragg−Brentano mode using a Smartlab Rigaku diffractometer, equipped with a rotating anode of Cu Kα radiation operating at 45 kV and 200 mA.

The morphology was analyzed by field-emission scanning electron microscopy (FE-SEM) using a ZEISS SUPRA 55 VP microscope. The atomic composition of the samples was determined by an energy dispersive X-ray (EDX) analysis. The EDX spectra were recorded using an INCA-Oxford windowless detector, having a resolution of 127 eV as the full width at half-maximum (fwhm) of the Mn Kα radiation.

2.3. Photocatalytic Test. The photocatalytic capabilities were tested through the degradation of rhodamine B (RhB) under a UV

lamp with $\lambda = 360$ nm and a 4000 K natural white LED lamp (150 W) at 25 °C. The light source was kept 15 cm away from the photocatalytic reactor. The power of the visible light at 15 cm was equal to 5 mW/cm^2. Typically, 0.15 g of the CsPbBr$_3$ powder was immersed into 5 mL aqueous solutions of RhB (1×10^{-6} M) in a beaker. In order to attain the adsorption/desorption balance of dye molecules on the CsPbBr$_3$ surfaces of the photocatalysts, the suspension was stirred for 30 min (min) in the dark. Thereafter, at regular intervals of 10 min, the solution was sampled by a JASCO V-650 UV−vis spectrophotometer to monitor the maximum wavelengths of the dye under irradiation.

3. RESULTS AND DISCUSSION

3.1. Phase Stability: CsPbBr$_3$ vs CsPb$_2$Br$_5$. The presently reported method represents a facile, one-step, low-temperature and surfactant-free approach for the synthesis of CsPbBr$_3$ and CsPb$_2$Br$_5$ phases. Optimization of the synthetic parameter conditions allows the production in a reproducible and selective way of the CsPbBr$_3$ or CsPb$_2$Br$_5$ microcrystals.

The synthetic approach of the present work is summarized in Scheme 1. Starting from a solution of Cs(hfa) and [Pb(hfa)$_2$·diglyme]$_2$ complexes in a 1:0.5 molar ratio, liquid bromine was added as a precipitating agent. The metal−organic complexes, in fact, are soluble in ethanol solution and partially precipitate as bromide phases upon addition of liquid bromine. A dynamic equilibrium takes place between the precursor solution, containing the cesium and lead complexes, and the crystal precipitates. This equilibrium allows control of the composition of the precipitate, which is partially soluble and thus still reactive. In fact, the precipitates, collected by filtration, washed in ethanol, and dried, show different compositions according to the aging time.

An in-depth XRD analysis was used to monitor the evolution of the two CsPbBr$_3$−CsPb$_2$Br$_5$ phases. The XRD pattern of the as-precipitated powder, immediately collected, displays stabilization of the CsPbBr$_3$ phase, while the powders aged from 5 to 20 h in solution at 60 °C are stabilized as the CsPb$_2$Br$_5$ phase (Scheme 1 and Figure 1).

All of the diffraction patterns of the dried microcrystalline powders have been collected as a function of aging time from $t = 0$ to $t = 20$ h in a stock solution (Figure 1). The first pattern collected at $t = 0$ (black line) points to the formation of the CsPbBr$_3$ perovskite, as confirmed by comparison with the powder diffraction file ICDD 18-0364. All of the peaks are present in the pattern, indicating no preferential orientation. A closer look at the pattern in Figure S1a allows the exclusion of the presence of any peaks associated with the CsPb$_2$Br$_5$ phase, while very few peaks, barely visible, are likely due to the presence of PbBr$_2$ impurities. The samples at longer aging times, i.e. $t = 5$, 10 h, also display peaks associated with the CsPb$_2$Br$_5$ phase (ICDD 25-0211), which gradually increases, resulting in a mixture of the two species. Finally, when the time is increased to 15 h, the intensities of peaks associated with the CsPb$_2$Br$_5$ are predominant and the signal of the CsPbBr$_3$ phase is barely visible. Thus, the powder obtained at 20 h displays the pattern associated with the CsPb$_2$Br$_5$ phase, while only traces of the CsPbBr$_3$ phase are observed. An additional graph is reported in Figure S1b, in which the pattern related to the powder at $t = 20$ h is compared with the corresponding simulated patterns. In all of the XRD analyses, the lack of a wide signal at around $2\theta = 20°$ points to the absence of amorphous phases. These findings indicate that at longer aging time the equilibrium between precipitates and precursors in the solution tends to stabilize the CsPb$_2$Br$_5$ phase.
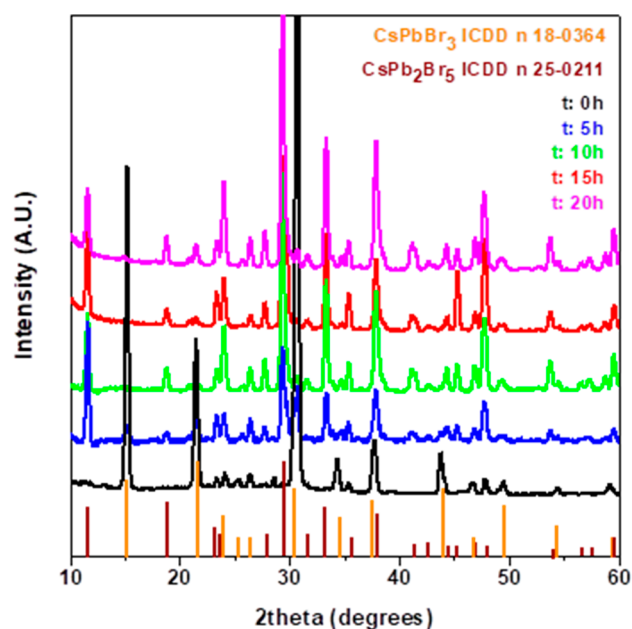

Figure 1. XRD patterns of CsPbBr$_3$/CsPb$_2$Br$_5$ crystals obtained at different aging times t: 0 h (black line), 5 h (blue line), 10 h (green line), 15 h (red line) and 20 h (pink line).

For the classical procedure reported in the literature, the transformation from CsPbBr$_3$ to CsPb$_2$Br$_5$ is due to an equilibrium between CsPbBr$_3$ and PbBr$_2$.[58]

A phase stability competition between CsPbBr$_3$ and CsPb$_2$Br$_5$ has already been addressed,[59−61] and the evolution from CsPbBr$_3$ nanocrystals to 2D CsPb$_2$Br$_5$ nanosheets has been the subject of investigation due to their luminescence properties.[62]

As it is crucial issue for the functional properties of these materials, a process that combines an accurate control of the phase formation by an easily scalable and fast synthetic approach represents a landmark in this inorganic halide perovskite field.

Furthermore, in order to understand the stability of the CsPbBr$_3$ phase in relation to temperature, we prepared a new set of samples in which the synthesis was carried out at $T = 60$ °C and crystals were collected at the aging time 0 h. Then, the crystals were annealed at 70 °C in air for 100 min. This test allows the study of the stability of the material under conditions that simulate those sustained by typical optoelectronic devices, i.e. sensor, photocatalyst, and PV panels, under irradiation in air. In Figure 2 the XRD patterns recorded at annealing treatments $t = 0$ min and $t = 100$ min are reported for comparison. After the annealing treatment, the peaks associated with the CsPbBr$_3$ phase are still present. Notably, by a comparison of these data with those obtained from the previous syntheses, it can be hypothesized that while the permanence of the product within the reaction mixture stabilizes the CsPb$_2$Br$_5$ phase in comparison to the CsPbBr$_3$ phase, the annealing treatment processes do not promote this transformation and tend to stabilize the CsPbBr$_3$ phase.

Additionally, dynamic thermogravimetric (TG) measurements on CsPb$_2$Br$_5$ and CsPbBr$_3$ microcrystals were carried out and are reported in Figure S2. The CsPb$_2$Br$_5$ and CsPbBr$_3$ systems both present an excellent stability of up to 500 °C with negligible weight losses up to 500 °C. The good thermal
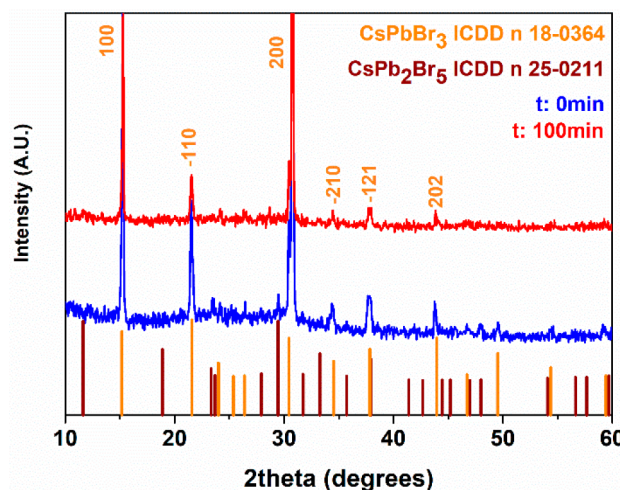
Figure 2. XRD patterns of $CsPbBr_3$ crystals obtained at aging time 0 h before (blue line) and after (red line) heat treatment at $T = 70$ °C for 100 min in air.

stability and the trend observed are in agreement with literature data.[63,64]

3.2. Morphological and Compositional Analysis. An in-depth morphological characterization has been carried out through FE-SEM analysis of the different products obtained as a function of the aging time (Figure 3). The FE-SEM image for the sample of $CsPbBr_3$ obtained at $t = 0$ h (Figure 3a) shows a homogeneous morphology of square grains in the dimension range of 1−3 μm. The shape of the crystals is quite regular, but the size distribution is not very narrow, as a consequence of the surfactant-free approach. The $CsPbBr_3$ shows by the naked eye an intense yellow-orange color (see inset in Figure 3 on the left), as already observed for this phase.[65] No significant change in terms of morphology has been observed for the $CsPbBr_3$−$CsPb_2Br_5$ sample at $t = 5$ h (Figure 3b). At longer aging times of 10 and 15 h as shown in Figure 3c,d, a change in morphology is evident, showing smaller and smoother grains. This effect is likely also due to the substantial change in the crystalline structure caused by the equilibrium with the precursor species present in the stock solution. Finally, the image obtained for a longer aging time of 20 h (Figure 3e) shows grains partially coalesced with irregular shapes and with smaller dimensions ranging between 600 nm and 2 μm. The final $CsPb_2Br_5$ crystals are pale yellow (see inset Figure 3 on

the right). This behavior could be explained by considering that a longer aging time leads to smaller and irregular crystals due to partial solubilization of the material and uncontrolled coalescence phenomena.

Finally, energy dispersive X-ray (EDX) point analyses within the grains confirm the difference in composition of the samples, in which the crystals obtained at $t = 0$ h have a Cs:Pb:Br ratio of about 1:0.9:3.2, correlated to the presence of the $CsPbBr_3$ phase (Figure 4, red line), while the crystals
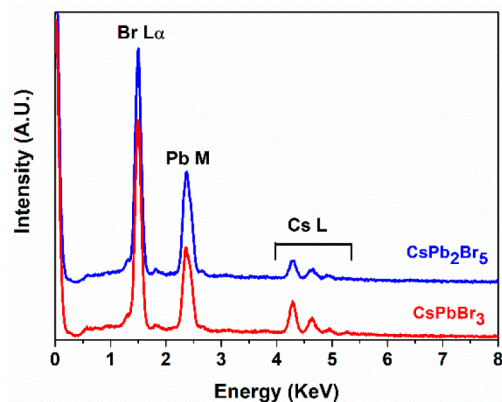
Sample	Quantitative analysis (atomic perc.)		
	Cs (L)	Pb (M)	Br (L)
$CsPb_2Br_5$	12.4%	23.1%	64.4%
$CsPbBr_3$	19.5%	18.4%	62.2%

Figure 4. EDX spectra of $CsPbBr_3$/$CsPb_2Br_5$ crystals obtained at aging time $t = 0$ h (red line) and 5 h (blue line).

obtained at $t = 5$ h have a Cs:Pb:Br ratio of about 1:1.9:5.2 due to the presence of the $CsPb_2Br_5$ phase (Figure 4, blue line). These data are in accordance with the XRD measurements and point out the stability of the $CsPbBr_3$ perovskite phase at $t = 0$ h and the predominance of $CsPb_2Br_5$ phase already at $t = 5$ h. Interestingly, no peak associated with carbon (0.27 keV) or fluorine (0.67 keV), which could arise from the Cs(hfa) and $[Pb(hfa)_2 \cdot diglyme]_2$ complexes, are present in either material, confirming the sample purity as a consequence of a clean decomposition process of the precursors. The absence of an oxygen signal at 0.52 keV, due to the formation of oxide phase
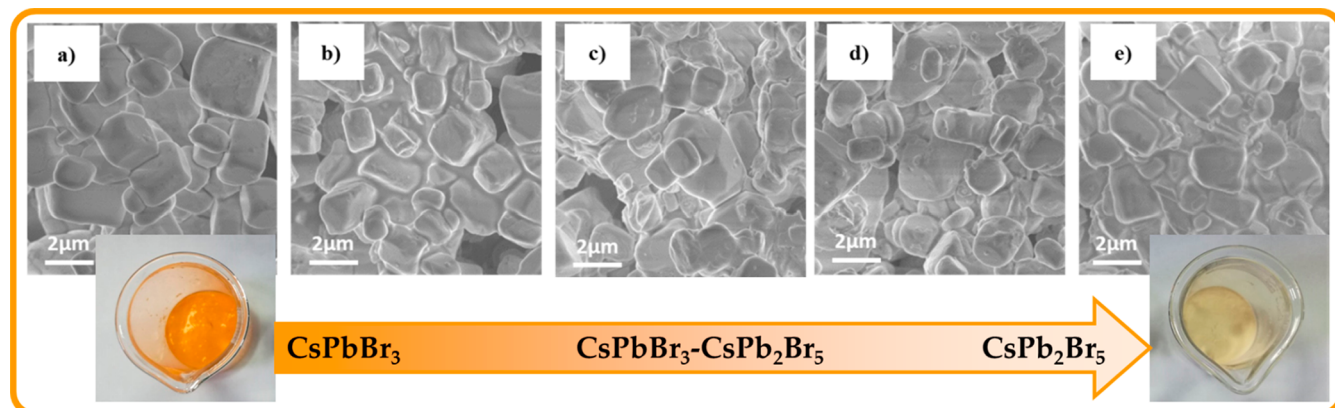

Figure 3. FE-SEM images of $CsPbBr_3$/$CsPb_2Br_5$ crystals obtained at aging time $t = 0$ h (a), 5 h (b), 10 h (c), 15 h (d), and 20 h (e).
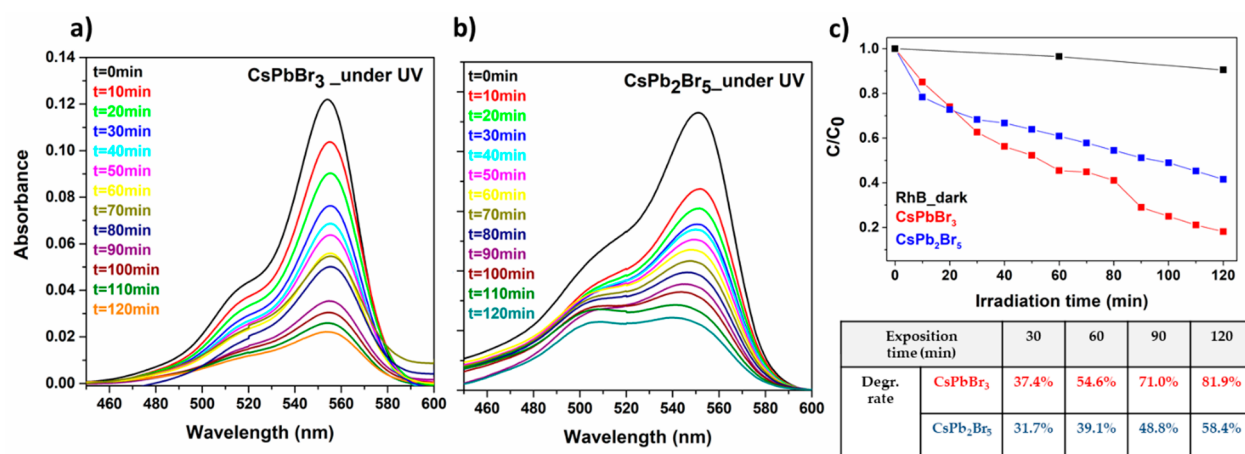
Figure 5. Visible spectra evolution of an RhB solution with (a) $CsPbBr_3$ and (b) $CsPb_2Br_5$ collected from 10 to 120 min obtained under a UV lamp (λ = 360 nm) and (c) concentration C/C_0 changes of RhB without and with $CsPbBr_3$ (red) and $CsPb_2Br_5$ (blue) catalysts under UV irradiation at different exposition times.
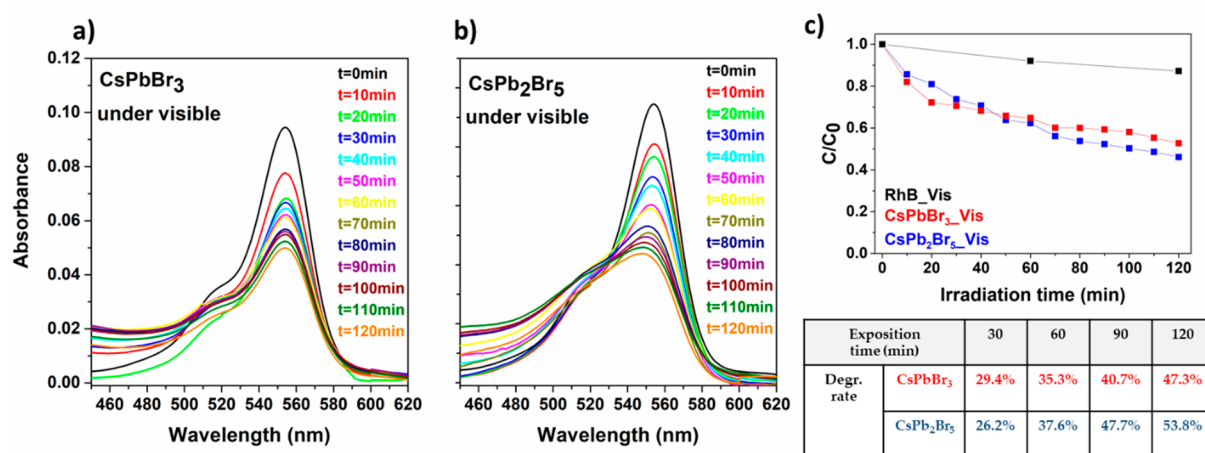

Figure 6. Visible spectra evolution of RhB solution with (a) $CsPbBr_3$ and (b) $CsPb_2Br_5$ collected from 10 to 120 min obtained under a visible-light lamp and (c) concentration C/C_0 changes of RhB without and with $CsPbBr_3$ (red) and $CsPb_2Br_5$ (blue) catalysts under visible-light irradiation at different exposition times.

byproducts, confirms the formation of pure bromide perovskite phases. Thus, this synthetic approach allows a fast and green production of $CsPbBr_3$ microcrystals without the need for any purification step after the precipitation.

3.3. Photocatalytic Properties. Preliminary tests on the photocatalytic properties of the $CsPbBr_3$ and $CsPb_2Br_5$ phases have been carried out using aqueous solutions of rhodamine B (RhB) under both a UV lamp (λ = 360 nm) and a visible-light lamp (natural white LED lamp, 150 W), with monitoring of the main absorption peak evolution at 553 nm of the RhB. Before the catalytic test was performed with the materials, the crystals were thoroughly washed in ethanol and dried overnight in order to eliminate any trace of contaminants such as Br_2 and unreacted precursors.

First, the stability of the $CsPbBr_3$ phase under UV irradiation was checked. For this reason, EDX measurements on the $CsPbBr_3$ crystals recorded before and after UV treatment in air for 120 min were conducted, confirming the stability of the $CsPbBr_3$ phase (Figure S3).

In addition, the degradation yield of the RhB solution was evaluated through UV and visible irradiation for 120 min. The percentage of degradation in absence of the catalyst species

was quantified as 9.5% and 12% after 120 min under UV and visible irradiation, respectively (Figure S4).

As shown in Figure 5a, the peak absorption evolution in the visible range of the RhB solution with suspended $CsPbBr_3$ was collected for every 10 min of UV irradiation. The bleaching of the solution is already visible by the naked eye after 60 min, and the decomposition process is almost linear (Figure 5c). The amoung of degradation is 37.4% after 30 min and reaches 54.6% and 71.0% after 60 and 90 min, respectively. After 120 min of the UV treatment, the degradation yield was up to 81.9%. In addition, an analogous test was conducted using $CsPb_2Br_5$ and is reported in Figure 5b. In this case, the degradation percentage is 31.7% after 30 min and reaches 39.1%, 48.8%, and 58.4% after 60, 90, and 120 min, respectively. The blue shift of the peak at 553 nm in Figure 5b can be attributed to dye dealkylation processes.[66,67]

A comparison of the degradation yields under the UV lamp in Figure 5c displays similar rates for the two samples in the first 30 min (37.4% for $CsPbBr_3$ vs 31.7% for $CsPb_2Br_5$) and a marked difference in the following 90 min.

Analogously, the absorbance evolution of the RhB solution with suspended $CsPbBr_3$ or $CsPb_2Br_5$ was evaluated under visible-light irradiation (natural white LED lamp ,150 W) for

Table 1. Comparison of Photocatalytic Performances of Cs-Pb-Br Systems in the Degradation of Organic Molecules under the Action of Different Irradiation Sources and Times
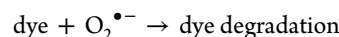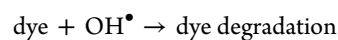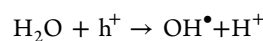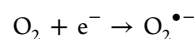
sample	irradiation source	time (min)	dye	degradation rate (%)	ref
$CsPbBr_3$ crystals	UV light ($\lambda = 360$ nm)	120	rhodamine B	81.9	this work
$CsPbBr_3$ crystals	LED light (150 W) (5 mW cm^{-2})	120	rhodamine B	47.3	this work
$CsPbBr_3$ QDs	Xe light (500 W)	80	methyl orange	82	39
$CsPbBr_3$ cubes		210	eosin B	82	40
$CsPbBr_3$ nanocrystals/PMMA fibrous membrane		60	methylene blue	99.18	69
$CsPbBr_3$ colloidal nanocrystal clusters	Xe light (410 mW cm^{-2})	60	methylene blue	100	70
$CsPbBr_3$ quantum dot glass	Xe light (450 W)	3 cycles of 60	antibiotic (TC-HCl)	85	71
$CsPb_2Br_5$ crystals	UV light ($\lambda = 360$ nm)	120	rhodamine B	58.4	this work
$CsPb_2Br_5$ crystals	LED light (150 W) (5mW cm^{-2})	120	rhodamine B	53.8	this work

120 min. In Figure 6a,b the evolution of the absorbance spectra of RhB dye is already visible after 30 min for both $CsPbBr_3$ and $CsPb_2Br_5$ systems and the decomposition process is almost linear (see Figure 6c). During the first 60 min of monitoring, the two dye solutions present a similar trend with degradation yields of 35.3% and 37.6% for $CsPbBr_3$ and $CsPb_2Br_5$, respectively. In the second hour of the process, an appreciable difference is indeed observed between the two phases with a final degradation yield of 47.3% for the $CsPbBr_3$ system and 53.8% for the $CsPb_2Br_5$ phase. Interestingly, a photocatalytic test executed on $CsPb_2Br_5$ presents a different trend in the evolution of the peak at 516 nm in the spectra (Figure 6b) in comparison to the $CsPbBr_3$ peak (Figure 6a). This effect could be likely associated with a partial decomposition of the dye that, due to demethylation processes, yields intermediates which may absorb light at higher energies.[68]

It is worth noting that several parameters could affect the degradation yield rate, such as the nature and the power of the irradiation source, the distance of the source from the solutions (i.e., the power/cm^2), the time of exposition, and the crystal shape and size, and thus a direct comparison with literature data is not so simple, since often not all of the aforementioned parameters have been reported. Nevertheless, in order to actually relate the present results within the state of the art panorama, we have compared the degradation ability of the present $CsPbBr_3$ and $CsPb_2Br_5$ crystals with those of analogous systems reported in the literature in the last few years (Table 1). In comparison with other catalyst systems, the photocatalytic performance of the $CsPbBr_3$ crystals reported herein is one of the most promising in the last few years. In fact, such a high catalytic efficiency was observed for $CsPbBr_3$ QDs by Gao et al. in degrading methyl orange solution using a much more powerful lamp (500 W),[39] and by Das at al. using eosin-B under visible light irradiation after a longer time of 210 min.[40] Higher performances have been reported only for the degradation of methylene blue in the case of $CsPbBr_3$ nanocrystals embedded in a PMMA fibrous membrane[69] and for a colloidal $CsPbBr_3$ system treated with more intense light sources.[70] Such high degradation rates have been recorded using a visible light source such as a Xe lamp characterized by about 2 orders of magnitude higher wattage (400 W cm^{-2}) and with different emission spectra with respect to the light source used for this work.[72] Conversely, the visible lamp tested herein is a natural white LED lamp of 150 W intensity, but with a real electrical consumption of 18 W, which has the advantage of being commercially available, cheap, and suitable for an indoor environment. Finally, a comment should be made about the self-degradation of methylene blue induced by visible-light

exposure (usually around 12−15%), which should be considered in the total degradation yield of the dye reported in the articles.

Finally, the photocatalysis mechanism can be explained according to ref 38 as follows:

$$Cs\text{-}Pb\text{-}AIHP \text{ crystals} + h\nu \rightarrow e^- + h^+$$

$$O_2 + e^- \rightarrow O_2^{\bullet-}$$

$$H_2O + h^+ \rightarrow OH^\bullet + H^+$$

$$dye + OH^\bullet \rightarrow dye \text{ degradation}$$

$$dye + O_2^{\bullet-} \rightarrow dye \text{ degradation}$$
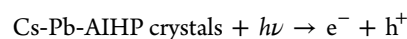
The process starts with the irradiation of an aqueous suspension of the catalyst species by light with energy higher than or equal to the band gap of the active materials, which leads to the formation of electrons in the conduction band and holes in valence bands. Hence, on the surface of Cs-Pb-AIHP crystals, oxygen may act as an electron acceptor producing $O_2^{\bullet-}$, while the holes react with the water molecules to form $OH^\bullet$ radicals. Thus, these highly reactive radicals oxidize the dye molecules.

A comment should be made regarding the stability of these structures in aqueous medium. It has been reported that the $CsPb_2Br_5$ phase exhibits excellent stability against humidity.[73,74] A few reports have shown some water effect on $CsPbBr_3$ stability, which may give rise to the formation of the $CsPb_2Br_5$ phase.[73] Nevertheless, in the literature there have been reports in which different systems, such as polymer-AIHP composite structures, have been successfully applied with the aim of enhancing the stability of the halide perovskite $CsPbBr_3$ in water.[33]

In general, these preliminary measurements evidence the promising photocatalytic properties of both the $CsPbBr_3$ and $CsPb_2Br_5$ phases, paving the way to their massive use as heterogeneous catalysts in the degradation processes of organic species. Furthermore, the use of a natural white LED lamp as the light source represents an innovative source, which paves the way to a novel strategy of photocatalytic processes, allowing the massive use of the setup herein.

In the field of photocatalysis, the results herein are fairly comparable with those for commonly reported inorganic systems, such as the metal oxides TiO_2, ZnO, and Fe_2O_3, showing excellent photocatalytic properties for similar applications.[75,76]

4. CONCLUSIONS

In summary, the approach herein represents the first report of a novel and facile acid-catalyzed green solution synthesis, which allows the production of $CsPbBr_3$ and $CsPb_2Br_5$ phases with a high control of composition and stability.

Among the advantages of the approach used is the reproducibility and selectivity of the synthetic methodology in producing $CsPbBr_3$ and $CsPb_2Br_5$ microcrystalline compounds. To our knowledge this represents the first study on the application of metal−organic Cs and Pb β-diketonate compounds, taking advantage of their reactivity and high solubility in low-impact organic solvents. The precipitation process takes place very rapidly after the addition of bromine in the reagent solution and does not require humidity control.

Furthermore, the reported approach not only represents an interesting green synthetic strategy, which avoids the use of surfactant species and toxic solvents, but also occurs at room temperature and is a very fast synthetic process. The stabilization of the $CsPbBr_3$ or the $CsPb_2Br_5$ phase involves an accurate investigation of the effect of process parameters such as aging time and annealing treatment on the evolution of the material composition and morphology.

In particular, the aging time plays a crucial role in the competition between the formation of the $CsPbBr_3$ and the $CsPb_2Br_5$ phases. Both $CsPbBr_3$ and $CsPb_2Br_5$ crystals show a good thermal stability, as assessed by an annealing treatment at 70 °C for different times and thermogravimetric analysis up to 500 °C. Also, the stability under a UV lamp has been confirmed. The FE-SEM analyses indicate that grain dimensions and shapes are related to the processing parameters, with square grains at time 0 h and grains with irregular rounded shapes and smaller dimensions at longer aging times.

As a proof of concept of the photocatalytic activity, preliminary measurements using an RhB solution indicate promising photocatalytic properties in dye degradation processes under visible irradiation, showing degradation rates of 47.3% for the $CsPbBr_3$ microcrystals and 53.8% for the $CsPb_2Br_5$ microcrystals. Conversely, under UV light, dye degradation processes reach higher values of up to 81.9% for the $CsPbBr_3$ phase and up to 58.4% for the $CsPb_2Br_5$ phase.

These results pave the way for more widely extended photocatalytic applications of Cs-Pb-Br systems, given both the straightforward synthetic strategy and the highly appealing photoactivity presently validated.

■ ASSOCIATED CONTENT

Ⓢ Supporting Information

The Supporting Information is available free of charge at https://pubs.acs.org/doi/10.1021/acsaem.1c01636.

> Structures of the cesium and lead precursors, XRD patterns of $CsPbBr_3$ and $CsPb_2Br_5$, thermogravimetric curves of the $CsPbBr_3$ and $CsPb_2Br_5$ crystals, EDX spectrum of $CsPbBr_3$ crystals after UV treatment, and visible spectra of the RhB solution before and after irradiation under a UV lamp (λ = 360 nm) and visible light (PDF)

■ AUTHOR INFORMATION

Corresponding Author

Anna Lucia Pellegrino − *Dipartimento di Scienze Chimiche, Università di Catania and INSTM UdR Catania, I-95125 Catania, Italy;* ⓞ orcid.org/0000-0001-5382-8205; Email: annalucia.pellegrino@unict.it

Author

Graziella Malandrino − *Dipartimento di Scienze Chimiche, Università di Catania and INSTM UdR Catania, I-95125 Catania, Italy;* ⓞ orcid.org/0000-0001-7483-3070

Complete contact information is available at: https://pubs.acs.org/10.1021/acsaem.1c01636

Author Contributions

Investigation, methodology, and writing (original draft preparation), A.L.P.; writing (review and editing), A.L.P. and G.M.; funding acquisition, G.M. Both authors have read and agreed to the published version of the manuscript.

Notes

The authors declare no competing financial interest.

■ REFERENCES

(1) Ma, C.-G.; Brik, M. G. Hybrid density-functional calculations of structural, elastic and electronic properties for a series of cubic perovskites $CsMF_3$ (M = Ca, Cd, Hg, and Pb). *Comput. Mater. Sci.* **2012**, *58*, 101−112.

(2) Jagadamma, L. K.; Edwards, P. R.; Martin, R. W.; Ruseckas, A.; Samuel, I. D. W. Nanoscale Heterogeneity in CsPbBr3 and CsPbBr3:KI Perovskite Films Revealed by Cathodoluminescence Hyperspectral Imaging. *ACS Appl. Energy Mater.* **2021**, *4*, 2707−2715.

(3) Zhi, R.; Hu, J.; Yang, S.; Perumal Veeramalai, C.; Zhang, Z.; Saleem, M. I.; Sulaman, M.; Tang, Y.; Zou, B. A facile method to synthesize two-dimensional $CsPb_2Br_5$ nano-/micro-sheets for high-performance solution-processed photodetectors. *J. Alloys Compd.* **2020**, *824*, 153970.

(4) Shao, G.; Zhao, Y.; Yu, Y.; Yang, H.; Liu, X.; Zhang, Y.; Xiang, W.; Liang, X. Bright emission and high photoluminescence $CsPb_2Br_5$ NCs encapsulated in mesoporous silica with ultrahigh stability and excellent optical properties for white light-emitting diodes. *J. Mater. Chem. C* **2019**, *7*, 13585−13593.

(5) Jin, M.; Li, Z.; Huang, F.; Wang, W. Electronic and optical properties of $CsPb_2Br_5$: A first-principles study. *Mod. Phys. Lett. B* **2019**, *33*, 1950266.

(6) Docampo, P.; Bein, T. A Long-Term View on Perovskite Optoelectronics. *Acc. Chem. Res.* **2016**, *49*, 339−46.

(7) Jaffe, B. *Piezoelectric ceramics*; Elsevier: 2012; Vol. 3.

(8) Kojima, A.; Teshima, K.; Shirai, Y.; Miyasaka, T. Organometal Halide Perovskites as Visible-Light Sensitizers for Photovoltaic Cells. *J. Am. Chem. Soc.* **2009**, *131*, 6050−6051.

(9) Gao, C.; Zhang, F.; Gu, X.; Huang, J.; Wang, K.; Zhang, S.; Liu, S.; Tian, Q. Versatile Bidentate Chemical Passivation on a Cesium Lead Inorganic Perovskite for Efficient and Stable Photovoltaics. *ACS Appl. Energy Mater.* **2021**, *4*, 4021.

(10) Catalano, M. R.; Spedalotto, G.; Condorelli, G. G.; Malandrino, G. MOCVD Growth of Perovskite Multiferroic $BiFeO_3$ Films: The Effect of Doping at the A and/or B Sites on the Structural, Morphological and Ferroelectric Properties. *Adv. Mater. Interfaces* **2017**, *4*, 1601025.

(11) Micard, Q.; Pellegrino, A. L.; Lo Nigro, R.; Bartasyte, A.; Condorelli, G. G.; Malandrino, G. Piezoelectric Ba and Ti co-doped

BiFeO$_3$ textured films: selective growth of solid solutions or nanocomposites. *J. Mater. Chem. C* **2020**, *8*, 16168−16179.

(12) Wang, J.; Wang, J.; Neaton, J. B.; Zheng, H.; Nagarajan, V.; Ogale, S. B. Epitaxial BiFeO$_3$ multiferroic thin-film heterostructures. *Science* **2003**, *299*, 1719−1722.

(13) Nimens, W. J.; Ogle, J.; Caruso, A.; Jonely, M.; Simon, C.; Smilgies, D.; Noriega, R.; Scarpulla, M.; Whittaker-Brooks, L. Morphology and Optoelectronic Variations Underlying the Nature of the Electron Transport Layer in Perovskite Solar Cells. *ACS Appl. Energy Mater.* **2018**, *1*, 602−615.

(14) Unlu, F.; Jung, E.; Haddad, J.; Kulkarni, A.; Oz, S.; Choi, H.; Fischer, T.; Chakraborty, S.; Kirchartz, T.; Mathur, S. Understanding the interplay of stability and efficiency in A-site engineered lead halide perovskites. *APL Mater.* **2020**, *8*, 070901.

(15) Ono, L. K.; Juarez-Perez, E. J.; Qi, Y. Progress on Perovskite Materials and Solar Cells with Mixed Cations and Halide Anions. *ACS Appl. Mater. Interfaces* **2017**, *9*, 30197−30246.

(16) Sanzaro, S.; Smecca, E.; Mannino, G.; Bongiorno, C.; Pellegrino, G.; Neri, F.; Malandrino, G.; Catalano, M. R.; Condorelli, G. G.; Iacobellis, R.; De Marco, L.; Spinella, C.; La Magna, A.; Alberti, A. Multi-Scale-Porosity TiO$_2$ scaffolds grown by innovative sputtering methods for high throughput hybrid photovoltaics. *Sci. Rep.* **2016**, *6*, 39509.

(17) Pellegrino, G.; D'Angelo, S.; Deretzis, I.; Condorelli, G. G.; Smecca, E.; Malandrino, G.; La Magna, A.; Alberti, A. From PbI$_2$ to MAPbI$_3$ through Layered Intermediates. *J. Phys. Chem. C* **2016**, *120*, 19768−19777.

(18) NREL. Best Research-Cell Efficiency Chart/Photovoltaic Research/NREL: https://www.nrel.gov/pv/cell-efficiency.html (Accessed Sept 21, 2020).

(19) Oz, S.; Jena, A. K.; Kulkarni, A.; Mouri, K.; Yokoyama, T.; Takei, I.; Unlu, F.; Mathur, S.; Miyasaka, T. Lead(II) Propionate Additive and a Dopant-Free Polymer Hole Transport Material for CsPbI$_2$Br Perovskite Solar Cells. *ACS Energy Letters* **2020**, *5*, 1292−1299.

(20) Sun, Q.; Ni, C.; Yu, Y.; Attique, S.; Wei, S.; Ci, Z.; Wang, J.; Yang, S. Design principle of all-inorganic halide perovskite-related nanocrystals. *J. Mater. Chem. C* **2018**, *6*, 12484−12484.

(21) Zhu, X.; Lin, Y.; Sun, Y.; Beard, M. C.; Yan, Y. Lead-Halide Perovskites for Photocatalytic α-Alkylation of Aldehydes. *J. Am. Chem. Soc.* **2019**, *141*, 733−738.

(22) Palei, M.; Imran, M.; Biffi, G.; Manna, L.; Di Stasio, F.; Krahne, R. Robustness to High Temperatures of Al$_2$O$_3$-Coated CsPbBr$_3$ Nanocrystal Thin Films with High-Photoluminescence Quantum Yield for Light Emission. *ACS Appl. Nano Mater.* **2020**, *3*, 8167−8175.

(23) Meng, L.; Yao, E. P.; Hong, Z.; Chen, H.; Sun, P.; Yang, Z.; Li, G.; Yang, Y. Pure Formamidinium-Based Perovskite Light-Emitting Diodes with High Efficiency and Low Driving Voltage. *Adv. Mater.* **2017**, *29*, 1603826.

(24) Veldhuis, S. A.; Boix, P. P.; Yantara, N.; Li, M.; Sum, T. C.; Mathews, N.; Mhaisalkar, S. G. Perovskite Materials for Light-Emitting Diodes and Lasers. *Adv. Mater.* **2016**, *28*, 6804−6834.

(25) Wang, W.; Ma, Y.; Qi, L. High-Performance Photodetectors Based on Organometal Halide Perovskite Nanonets. *Adv. Funct. Mater.* **2017**, *27*, 1603653.

(26) Saidaminov, M. I.; Adinolfi, V.; Comin, R.; Abdelhady, A. L.; Peng, W.; Dursun, I.; Yuan, M.; Hoogland, S.; Sargent, E. H.; Bakr, O. M. Planar-integrated single-crystalline perovskite photodetectors. *Nat. Commun.* **2015**, *6*, 8724.

(27) Huang, Z.; Ma, B.; Wang, H.; Li, N.; Liu, R. T.; Zhang, Z. Q.; Zhang, X. D.; Zhao, J. H.; Zheng, P. Z.; Wang, Q.; Zhang, H.-L. In Situ Growth of 3D/2D (CsPbBr$_3$/CsPb$_2$Br$_5$) Perovskite Heterojunctions toward Optoelectronic Devices. *J. Phys. Chem. Lett.* **2020**, *11*, 6007−6015.

(28) Zhang, Q.; Su, R.; Liu, X.; Xing, J.; Sum, T. C.; Xiong, Q. High-Quality Whispering-Gallery-Mode Lasing from Cesium Lead Halide Perovskite Nanoplatelets. *Adv. Funct. Mater.* **2016**, *26*, 6238−6245.

(29) Saris, S.; Loiudice, A.; Mensi, M.; Buonsanti, R. Exploring energy transfer in a metal/perovskite nanocrystal antenna to drive photocatalysis. *J. Phys. Chem. Lett.* **2019**, *10*, 7797−7803.

(30) Huang, H.; Pradhan, B.; Hofkens, J.; Roeffaers, M.B. J.; Steele, J. A. Solar-driven metal halide perovskite photocatalysis: design, stability, and performance. *ACS Energy Lett.* **2020**, *5*, 1107−1123.

(31) Baranov, D.; Caputo, G.; Goldoni, L.; Dang, Z.; Scarfiello, R.; De Trizio, L.; Portone, A.; Fabbri, F.; Camposeo, A.; Pisignano, D.; Manna, L. Transforming colloidal Cs$_4$PbBr$_6$ nanocrystals with poly(maleic anhydride-alt-1-octadecene) into stable CsPbBr$_3$ perovskite emitters through intermediate heterostructures. *Chem. Sci.* **2020**, *11*, 3986−3995.

(32) Akbulatov, A. F.; Luchkin, S. Y.; Frolova, L. A.; Dremova, N. N.; Gerasimov, K. L.; Zhidkov, I. S.; Anokhin, D. V.; Kurmaev, E. Z.; Stevenson, K. J.; Troshin, P. A. Probing the Intrinsic Thermal and Photochemical Stability of Hybrid and Inorganic Lead Halide Perovskites. *J. Phys. Chem. Lett.* **2017**, *8*, 1211−1218.

(33) Jiang, G.; Guhrenz, C.; Kirch, A.; Sonntag, L.; Bauer, C.; Fan, X.; Wang, J.; Reineke, S.; Gaponik, N.; Eychmüller, A. Highly Luminescent and Water-Resistant CsPbBr$_3$-CsPb$_2$Br$_5$ Perovskite Nanocrystals Coordinated with Partially Hydrolyzed Poly(methyl methacrylate) and Polyethylenimine. *ACS Nano* **2019**, *13*, 10386−10396.

(34) Tang, M. C.; Barrit, D.; Munir, R.; Li, R.; Barbé, J. M.; Smilgies, D.-M.; Del Gobbo, S.; Anthopoulos, T. D.; Amassian, A. Bismuth-Based Perovskite-Inspired Solar Cells: In Situ Diagnostics Reveal Similarities and Differences in the Film Formation of Bismuth- and Lead-Based Films. *Sol. RRL* **2019**, *3*, 1800305.

(35) Jin, Z.; Zhang, Z.; Xiu, J.; Song, H.; Gatti, T.; He, Z. A critical review on bismuth and antimony halide based perovskites and their derivatives for photovoltaic applications: recent advances and challenges. *J. Mater. Chem. A* **2020**, *8*, 16166−16188.

(36) Li, X.; Cao, F.; Yu, D.; Chen, J.; Sun, Z.; Shen, Y.; Zhu, Y.; Wang, L.; Wei, Y.; Wu, Y.; Zeng, H. B. All Inorganic Halide Perovskites Nanosystem: Synthesis, Structural Features, Optical Properties and Optoelectronic Applications. *Small* **2017**, *13*, 1603996.

(37) Zu, Y.; Dai, J.; Li, L.; Yuan, F.; Chen, X.; Feng, Z.; Li, K.; Song, X.; Yun, F.; Yu, Y.; Jiao, B.; Dong, H.; Hou, X.; Ju, M.; Wu, Z. Ultra-stable CsPbBr$_3$ nanocrystals with near-unity photoluminescence quantum yield via postsynthetic surface engineering. *J. Mater. Chem. A* **2019**, *7*, 26116−26122.

(38) Wang, Q.; Smith, J. A.; Skroblin, D.; Steele, J. A.; Wolff, C. M.; Caprioglio, P.; Stolterfoht, M.; Köbler, H.; Li, M.; Turren-Cruz, S. H.; Gollwitzer, C.; Neher, D.; Abate, A. Managing Phase Purities and Crystal Orientation for High-Performance and Photostable Cesium Lead Halide Perovskite Solar Cells. *Sol. RRL* **2020**, *4*, 2000213.

(39) Gao, G.; Xi, Q.; Zhou, H.; Zhao, Y.; Wu, C.; Wang, L.; Guo, P.; Xu, J. Novel inorganic perovskite quantum dots for photocatalysis. *Nanoscale* **2017**, *9*, 12032−12038.

(40) Das, S.; Paul, T.; Maiti, S.; Chattopadhyay, K. Ambient processed CsPbX$_3$ perovskite cubes for photocatalysis. *Mater. Lett.* **2020**, *267*, 127501.

(41) Cardenas-Morcoso, D.; Gualdrón-Reyes, A. F.; Ferreira Vitoreti, A. B.; García-Tecedor, M.; Yoon, S. J.; Solis De La Fuente, M.; Mora-Seró, I.; Gimenez, S. Photocatalytic and Photoelectrochemical Degradation of Organic Compounds with All-Inorganic Metal Halide Perovskite Quantum Dots. *J. Phys. Chem. Lett.* **2019**, *10*, 630−636.

(42) Harisingh, S.; Ramakrishnan, S.; Kulbak, M.; Levine, I.; Cahen, D.; El Cohen, B.; Etgar, L.; Asscher, M. CsPbBr$_3$ and CH$_3$NH$_3$PbBr$_3$ promote visible-light photo-reactivity. *Phys. Chem. Chem. Phys.* **2018**, *20*, 16847−16852.

(43) Shao, G.; Zhao, Y.; Yu, Y.; Yang, H.; Liu, X.; Zhang, Y.; Xiang, W.; Liang, X. Bright emission and high photoluminescence CsPb$_2$Br$_5$ NCs encapsulated in mesoporous silica with ultrahigh stability and excellent optical properties for white light-emitting diodes. *J. Mater. Chem. C* **2019**, *7*, 13585−13593.

(44) Zhu, X.; Lin, Y.; San Martin, J.; Sun, Y.; Zhu, D.; Yan, Y. Lead halide perovskites for photocatalytic organic synthesis. *Nat. Commun.* **2019**, *10*, 2843.

(45) Shyamal, S.; Dutta, S. K.; Das, T.; Sen, S.; Chakraborty, S.; Pradhan, N. Facets and defects in perovskite nanocrystals for photocatalytic CO_2 reduction. *J. Phys. Chem. Lett.* **2020**, *11*, 3608–3614.

(46) Kumar, S.; Regue, M.; Isaacs, M. A.; Freeman, E.; Eslava, S. All-Inorganic $CsPbBr_3$ Nanocrystals: Gram-Scale Mechanochemical Synthesis and Selective Photocatalytic CO_2 Reduction to Methane. *ACS Appl. Energy Mater.* **2020**, *3*, 4509–4522.

(47) Cho, M. Y.; Kim, S.; Kim, I. S.; Kim, E. S.; Wang, Z. J.; Kim, N. Y.; Kim, S. W.; Oh, J. M. Perovskite-Induced Ultrasensitive and Highly Stable Humidity Sensor Systems Prepared by Aerosol Deposition at Room Temperature. *Adv. Funct. Mater.* **2020**, *30*, 1907449.

(48) Huang, D.; Xie, P.; Pan, Z.; Rao, H.; Zhong, X. One-step solution deposition of $CsPbBr_3$ based on precursor engineering for efficient all-inorganic perovskite solar cells. *J. Mater. Chem. A* **2019**, *7*, 22420–22428.

(49) Duan, Y.; Zhao, G.; Liu, X.; Ma, J.; Chen, S.; Song, Y.; Pi, X.; Yu, X.; Yang, D.; Zhang, Y.; Guo, F. Highly efficient and stable inorganic $CsPbBr_3$ perovskite solar cells via vacuum co-evaporation. *Appl. Surf. Sci.* **2021**, *562*, 150153.

(50) Wang, H.; Wu, Y.; Ma, M.; Dong, S.; Li, Q.; Du, J.; Zhang, H.; Xu, Q. Pulsed Laser Deposition of $CsPbBr_3$ Films for Application in Perovskite Solar Cells. *ACS Appl. Energy Mater.* **2019**, *2*, 2305–2312.

(51) Cheng, J.; Yuan, S.; Zhu, L.; Chen, L.; Liu, C.; Tong, H.; Zeng, H. Room-Temperature In Situ Synthesis of a Highly Efficient $CsPbBr_3/SiO_2$ Sol Entirely in Ethanol Solvent by Constructing Amine-Functionalized Silica Micelles. *Langmuir* **2020**, *36*, 6017–6024.

(52) Cao, X.; Zhang, G.; Cai, Y.; Jiang, L.; He, X.; Zeng, Q.; Wei, J.; Jia, Y.; Xing, G.; Huang, W. All Green Solvents for Fabrication of $CsPbBr_3$ Films for Efficient Solar Cells Guided by the Hansen Solubility Theory. *Solar RRL* **2020**, *4*, 2000008.

(53) Wang, R.; Li, Z.; Li, S.; Wang, P.; Xiu, J.; Wei, G.; Liu, H.; Jiang, N.; Liu, Y.; Zhong, M. All-Inorganic Perovskite $CsPb_2Br_5$ Nanosheets for Photodetector Application Based on Rapid Growth in Aqueous Phase. *ACS Appl. Mater. Interfaces* **2020**, *12*, 41919–41931.

(54) Li, J.; Zhao, H.; Li, J.; Zheng, C.; Li, M.; Wang, S.; Ren, K.; Zhang, Y.; Yao, J. Photoresponse properties and energy gap of $CsPbBr_3$-$CsPb_2Br_5$ compound thin film prepared by one-step thermal evaporation method. *J. Mater. Sci.: Mater. Electron.* **2020**, *31*, 4956–4962.

(55) Leyden, M. R.; Jiang, Y.; Qi, Y. Chemical vapor deposition grown formamidinium perovskite solar modules with high steady state power and thermal stability. *J. Mater. Chem. A* **2016**, *4*, 13125–13132.

(56) Malandrino, G.; Lo Nigro, R.; Rossi, P.; Dapporto, P.; Fragalà, I. L. A volatile Pb(II) β- Diketonate diglyme complex as a promising precursor for MOCVD of lead oxide films. *Inorg. Chim. Acta* **2004**, *357*, 3927–3933.

(57) Vikulova, E. S.; Zherikova, K. V.; Kuratieva, N. V.; Morozova, N. B.; Igumenov, I. K. Synthesis, structure, and thermal properties of fluorinated cesium beta-diketonates. *J. Coord. Chem.* **2013**, *66*, 2235–2249.

(58) Shi, J.; Tian, Y.; Gao, W.; Xu, M.; Wu, Y.; Ge, W. Formulation of Water-Resistant Fluorescent Ink from Novel Octagonal $CsPbBr_3$/$CsPb_2Br_5$ Composite Plates Coordinated with Thermoplastic Polyurethane. *ACS Appl. Electron. Mater.* **2021**, *3*, 1413–142.

(59) Li, J.; Hu, M.; Wang, Z.; Lu, Y.; Wang, K.; Zhu, X. The scaling of the ligand concentration and Soret effect induced phase transition in $CsPbBr_3$ perovskite quantum dots. *J. Mater. Chem. A* **2019**, *7*, 27241–27246.

(60) Palazon, F.; Ajjouri, Y. E.; Sebastia-Luna, P.; Lauciello, S.; Manna, L.; Bolink, H. J. Mechanochemical synthesis of inorganic halide perovskites: evolution of phase-purity, morphology, and photoluminescence. *J. Mater. Chem. C* **2019**, *7*, 11406–11410.

(61) Li, G.; Wang, H.; Zhu, Z.; Chang, Y.; Zhang, T.; Song, Z.; Jiang, Y. Shape and phase evolution from $CsPbBr_3$ perovskite nanocubes to tetragonal $CsPb_2Br_5$ nanosheets with an indirect bandgap. *Chem. Commun.* **2016**, *52*, 11296–11299.

(62) Acharyya, P.; Pal, P.; Samanta, P. K.; Sarkar, A.; Pati, S. K.; Biswas, K. Single pot synthesis of indirect band gap 2D $CsPb_2Br_5$ nanosheets from direct band gap 3D $CsPbBr_3$ nanocrystals and the origin of their luminescence properties. *Nanoscale* **2019**, *11*, 4001–4007.

(63) Boote, B. W.; Andaraarachchi, H. P.; Rosales, B. A.; Blome-Fernandez, R.; Zhu, F.; Reichert, M. D.; Santra, K.; Li, J.; Petrich, J. W.; Vela, J.; Smith, E. A. Unveiling the Photo- and Thermal-Stability of Cesium Lead Halide Perovskite Nanocrystals. *ChemPhysChem* **2019**, *20*, 2647–2656.

(64) Palazon, F.; Dogan, S.; Marras, S.; Locardi, F.; Nelli, I.; Rastogi, P.; Ferretti, M.; Prato, M.; Krahne, R.; Manna, L. From $CsPbBr_3$ Nano-Inks to Sintered $CsPbBr_3$-$CsPb_2Br_5$ Films via Thermal Annealing: Implications on Optoelectronic Properties. *J. Phys. Chem. C* **2017**, *121*, 11956–11961.

(65) Huang, S.; Li, Z.; Wang, B.; Zhu, N.; Zhang, C.; Kong, L.; Zhang, Q.; Shan, A.; Li, L. Morphology Evolution and Degradation of $CsPbBr_3$ Nanocrystals under Blue Light-Emitting Diode Illumination. *ACS Appl. Mater. Interfaces* **2017**, *9*, 7249–7258.

(66) Chen, T.; Zheng, Y.; Lin, J.; Chen, G. Study on the Photocatalytic Degradation of Methyl Orange in Water Using Ag/ZnO as Catalyst by Liquid Chromatography Electrospray Ionization Ion-Trap Mass Spectrometry. *J. Am. Soc. Mass Spectrom.* **2008**, *19*, 997–1003.

(67) Sundararajan, M.; Sailaja, V.; Kennedy, L.; John, V.; Judith, J. Photocatalytic degradation of rhodamine B under visible light using nanostructured zinc doped cobalt ferrite: Kinetics and mechanism. *Ceram. Int.* **2017**, *43*, 540–548.

(68) Rochkind, M.; Pasternak, S.; Paz, Y. Using dyes for evaluating photocatalytic properties: a critical review. *Molecules* **2015**, *20*, 88.

(69) Zhang, Q.; Deng, X.; Tan, C.; Zhou, Y.; Chen, X.; Bai, X.; Li, J.; Tang, B.; Li, S.; Lin, H. Gamma-phase $CsPbBr_3$ perovskite nanocrystals/polymethyl methacrylate electrospun nanofibrous membranes with superior photo-catalytic property. *J. Chem. Phys.* **2020**, *153*, 024703.

(70) Hu, H.; Chen, M.; Yao, N.; Wu, L.; Zhong, Q.; Song, B.; Cao, M.; Zhang, Q. Highly Stable $CsPbBr_3$ Colloidal Nanocrystal Clusters as Photocatalysts in Polar Solvents. *ACS Appl. Mater. Interfaces* **2021**, *13*, 4017–4025.

(71) Li, P.; Lu, Y.; Duan, Y.; Xu, S.; Zhang, J. Potential Application of Perovskite Glass Material in Photocatalysis Field. *J. Phys. Chem. C* **2021**, *125*, 2382.

(72) Kim, S.; Jahandar, M.; Jeong, J. H.; Lim, D. C. Recent Progress in Solar Cell Technology for Low-Light Indoor Applications. *Current Alternative Energy* **2018**, *2*, 1–15.

(73) Turedi, B.; Lee, K. J.; Dursun, I.; Alamer, B.; Wu, Z.; Alarousu, E.; Mohammed, O. F.; Cho, N.; Bakr, O. M. Water-Induced Dimensionality Reduction in Metal-Halide Perovskites. *J. Phys. Chem. C* **2018**, *122*, 14128–14134.

(74) Ruan, L.; Shen, W.; Wang, A.; Xiang, A.; Deng, Z. Alkyl-Thiol Ligand-Induced Shape- and Crystalline Phase-Controlled Synthesis of Stable Perovskite-Related $CsPb_2Br_5$ Nanocrystals at Room Temperature. *J. Phys. Chem. Lett.* **2017**, *8*, 3853–3860.

(75) Din, M. I.; Khalid, R.; Najeeb, J.; Hussain, Z. Fundamentals and photocatalysis of methylene blue dye using various nanocatalytic assemblies- a critical review. *J. Cleaner Prod.* **2021**, *298*, 126567.

(76) Rafiq, A.; Ikram, M.; Ali, S.; Niaz, F.; Khan, M.; Khan, Q.; Maqbool, M. Photocatalytic degradation of dyes using semiconductor photocatalysts to clean industrial water pollution. *J. Ind. Eng. Chem.* **2021**, *97*, 111–128.